Anisotropic hot flow of textured Ti-6Al-4V sheet and its modification by superplastic pre-straining under hot stamping conditions

Famin Tian, Hao Wu and Nan Li*

Dyson School of Design Engineering, Imperial College London, Imperial College Road, South Kensington, London SW7 2DB, UK

* Corresponding author: Nan Li. E-mail: n.li09@imperial.ac.uk

Abstract

The effects of crystallographic texture and macrozones on the hot flow behaviour of a 1.6 mm Ti-6Al-4V sheet, and their modification by superplastic pre-straining, were investigated by uniaxial tensile testing at 900 °C and 1 s^{-1}, conditions representative of hot stamping. Directly heated (DH) specimens tested along the rolling, diagonal and transverse directions showed direction-dependent peak stress and flow softening: the transverse direction, along which most basal poles lie, gave the highest peak stress, whereas the diagonal direction softened least. Post-test SEM and EBSD revealed clusters of differently deformed primary α grains, Schmid-factor distributions and geometrically necessary dislocation (GND) patterns consistent with heterogeneous deformation associated with the macrozone structure. In a second route combining direct heating and superplastic pre-straining (DHS), pre-strains of 0.15 and 0.24 were applied at 900 °C and 10^{-3} s^{-1} before the subsequent 1 s^{-1} test, with total time at temperature matched to the DH route. Pre-straining weakened the basal texture, shifted the boundary population towards higher misorientations, slightly refined primary α grains and reduced residual GND density. During subsequent rapid deformation, the pre-strained sheet exhibited higher peak stress, less early softening and higher GND densities over the sampled strain interval, while the 0.24 pre-strain reduced local fracture strain. The results suggest superplastic pre-conditioning as a potential means of suppressing early flow softening in Ti-6Al-4V sheet.

Keywords: Ti-6Al-4V; hot stamping; texture; macrozones; flow softening; geometrically necessary dislocations

1. Introduction

The demand for lighter aircraft components has encouraged the use of thin-walled, complex-shaped parts made from titanium alloys with high specific strength [1]. Ti-6Al-4V is widely used for such applications, but forming complex sheet components by superplastic forming or isothermal hot forming can require substantial processing time and energy [2,3]. Faster approaches, including hot stamping with resistance or rapid heating [4,5] and Fast light Alloys Stamping Technology [6] have therefore been investigated to improve forming efficiency [7,8], and the flow and microstructural response of Ti-6Al-4V at hot stamping temperatures and strain rates has been examined in several studies [9–12] .

Industrial Ti-6Al-4V sheet processing commonly involves rolling below the β transus temperature, producing crystallographic texture and regions of similarly oriented primary α grains, referred to as macrozones [13]. Hot-tensile experiments by Gao et al. showed texture-induced anisotropy in the response of cold-rolled Ti-6Al-4V sheet and linked it to orientation dispersion, recovery and phase transformation [14]. da Silva et al. found that the directional differences of textured Ti-6Al-4V persisted at 750 °C regardless of strain rate but diminished at 900 °C under superplastic rates, where grain boundary sliding dominated [15]; whether they persist at 900 °C under the much faster rates of hot stamping has not been established. Zeng et al. demonstrated that rolling temperature, strain and reheating schedule affect α and β textures and macrozone development [16]. These findings motivate considering texture together with the thermal and deformation history when designing sheet microstructures for hot stamping.

Several mechanisms have been proposed to explain flow softening during hot deformation of titanium alloys, including dynamic recovery, recrystallisation, dynamic phase transformation, deformation heating, globularisation and texture evolution [17–22]. Recent work has coupled dynamic recrystallisation with texture evolution during hot deformation of Ti-6Al-4V [23], and the competition between dynamic softening and hardening during its hot deformation has been analysed as a multi-mechanism coupling [24]. Qu et al. identified continuous dynamic recrystallisation as the dominant restoration process under such conditions [9], and Kopec et al. examined Ti-6Al-4V under hot stamping conditions and related its flow behaviour to the evolving microstructure and phase balance [10]. The influence of phase transformation on flow softening has also been investigated using a step-quenching treatment before deformation [11,12,25]. These studies show that flow softening can reflect several simultaneous microstructural changes rather than a single mechanism.

Semiatin and Bieler reported a second-order contribution from texture to anisotropic hot flow and softening in Ti-6Al-4V under the investigated conditions [26]. More recently, Levkulich and Semiatin found that texture evolution explained only about one fifth of the measured softening in colony Ti-6Al-4V, with deformation heating and substructure evolution accounting for the remainder [27]. The spatial grouping of orientations also matters: macrozones and crystallographic orientation control slip activation and the anisotropic response of Ti-6Al-4V even under impact loading [28], and grain-scale strain localisation has been resolved by in-situ testing combined with crystal-plasticity modelling [29]. Experiments have associated microtextured regions with strain localisation [30], and crystal-plasticity modelling has examined how internal misorientation affects localisation within macrozones [31]. Lunt et al. showed that neighbourhood texture influences slip activity [32], while in-situ observations by Meng et al. identified orientation-dependent macrozone rotation and segmentation [33]. These works support a spatial microtexture perspective, while their different processing conditions preclude direct quantitative transfer to rapid hot forming.

In the α phase, deformation by basal and prismatic ⟨a⟩ slip is generally easier than deformation requiring pyramidal ⟨c+a⟩ slip [34]. Slip-system-specific critical resolved shear stresses measured recently confirm this hierarchy [35]. Transfer of deformation between favourably and unfavourably oriented grains can be restricted, leading to dislocation accumulation and stress concentrations at grain boundaries [36,37]. Deformation incompatibility between neighbouring grains in itself enhances the anisotropy of the stress–strain response of titanium [38], and microstructure-dependent slip activation and transfer govern the strength–ductility balance of Ti-6Al-4V [39]. Within a macrozone, neighbouring grains with similar orientations may permit more compatible slip transfer than a collection of randomly oriented grains. Reducing the spatial extent of these regions could therefore reduce the effective slip length and increase the number of barriers encountered by moving dislocations.

Superplastic deformation in Ti-6Al-4V can modify the orientation distribution through grain boundary sliding and grain rotation [2,40]. Yang and Wu examined grain-rotation-accommodated sliding, and subsequent work linked continuous dynamic recrystallisation to boundary evolution and subgrain rotation [41,42]. In a near-α titanium alloy, Xu et al. combined spheroidisation of a Widmannstätten starting structure with superplastic deformation to eliminate macrozones [43]. Macrozone fragmentation has likewise been used to improve the plastic stability of a near-α alloy [44]. The transverse texture of rolled sheet can also be weakened by asymmetric rolling with recrystallisation annealing before the sheet reaches the

forming press [45], or by boron microalloying [46]. Superplastic grain rotation and macrozone disruption are therefore established concepts; what a particular pretreatment does to subsequent forming must be assessed together with its other microstructural impacts.

A direct precedent for pre-strain-dependent tensile properties is the work of Wu et al., who used 850 °C and 10^{-3} s^{-1} for both deformation stages, separated by holding, quenching and reheating [47]. Among pre-strains of 0.05-0.15, 0.05 gave the highest strength and elongation.

The present study addresses two linked questions in a textured, equiaxed Ti-6Al-4V sheet under a condition representative of hot stamping (900 °C, 1 s^{-1}). First, how the anisotropy of flow stress and flow softening is governed by the rolling texture and macrozones, and how this is expressed in the post-deformation grain morphology, slip-system favourability and dislocation storage; second, whether a short superplastic pre-strain of 0.15-0.24 at 10^{-3} s^{-1}, applied with the total time at temperature held constant, can change the starting microstructure enough to alter the subsequent softening. The slow-then-fast sequence distinguishes this work from pre-strain studies in which both stages were carried out at the same low rate [47], from routes that remove macrozones by spheroidising a lamellar structure [43], and from sheet-processing routes that weaken the transverse texture before forming [45,46]. Texture, grain size, boundary character and residual dislocation content change together during the pre-strain, and the two pre-strain routes differ in their post-strain hold, which forms part of the processing history. These are treated as coupled variables; the aim is to establish whether the combined change is beneficial at stamping rates and which of its components the microstructural evidence favours.

2. Material and experimental methods

2.1. Material and specimen design

The Ti-6Al-4V material was supplied by Doncasters Group as a 1.6 mm thick sheet with a marked rolling direction and a β transus temperature of 995 °C. Its chemical composition is given in Table 1. Dog-bone specimens with a 30 × 6 mm parallel section were laser cut with their tensile axes parallel to the rolling direction (RD), the diagonal direction (DD, at 45° to RD) and the transverse direction (TD), as shown in Fig. 1.

Table 1. Chemical composition of the Ti-6Al-4V sheet (wt%).

Al	V	Fe	C	N	O	H	Ti
6.062	4.090	0.115	0.006	0.030	0.176	0.004	Balance

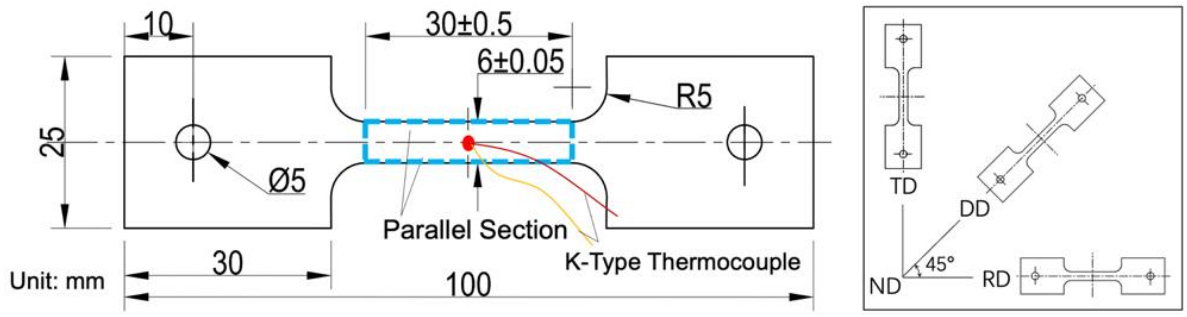

Fig. 1. Specimen design for the uniaxial tensile tests (RD, DD, TD and ND indicate rolling, diagonal, transverse and normal directions). The parallel section is 30 mm long and 6 mm wide; the sheet thickness is 1.6 mm.

2.2. High-temperature uniaxial tensile tests

Two sets of uniaxial tensile tests were conducted at 900 °C and a nominal constant true strain rate of 1 s^{-1} (Fig. 2). The first set used direct heating (DH) to examine the anisotropic flow of the as-received sheet along RD, DD and TD; these tests are denoted DH-RD, DH-DD and DH-TD. In the second set, the pretreatment combined direct heating with superplastic pre-straining (DHS) at 900 °C and 10^{-3} s^{-1} along RD before the final tensile test along RD. This combination of temperature, strain rate and fine initial equiaxed grain size (~6 μm) lies within the well-documented superplastic regime of Ti-6Al-4V, in which grain boundary sliding accommodated by grain rotation dominates [2,40]; the boundary character and texture changes reported later in this paper are consistent with this regime. Pre-strains of 0.15 and 0.24 were used for the subsequent flow comparison, denoted as DHS-0.15-RD and DHS-0.24-RD.

The DH specimens were soaked at 900 °C for 300 s before deformation. The DHS specimens were soaked for 30 s, pre-strained to the prescribed level of 0.15 and 0.24 and then unloaded during a further soak before the final tensile test (Table 2). For the pre-strain specimens, the total time at 900 °C before the final test was also 300 s, i.e. the same as for the DH route, although the two routes differ in the unloaded hold after pre-straining (120 s and 30 s). Additional pretreatment characterisation was carried out for pre-strains of 0.5 and 1.0 (Table 2); their longer total times at 900 °C (560 s and 1060 s) make them ancillary characterisation points, and they are not included in the matched-exposure flow comparison.

Table 2. Parameters of the DHS pretreatments. Pre-straining was performed at 900 °C and 10^{-3} s^{-1} after an initial 30 s soak; t_p is the pre-straining duration and t_s the unloaded soak after pre-straining.

Pre-strain	**t_p (s)**	**t_s (s)**	**Total time at 900 °C (s)**	**Use**
0.15	150	120	300	Flow comparison and characterisation

Pre-strain	t_p (s)	t_s (s)	Total time at 900 °C (s)	Use
0.24	240	30	300	Flow comparison and characterisation
0.5	500	30	560	Pretreatment characterisation only
1.0	1000	30	1060	Pretreatment characterisation only

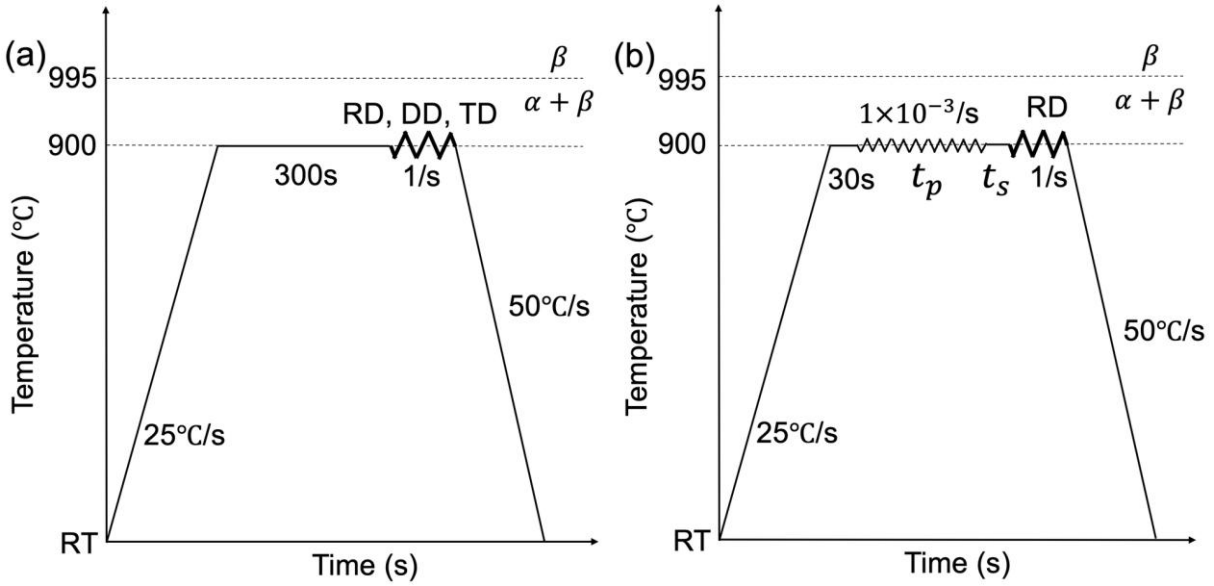

Fig. 2. Temperature profiles of the uniaxial tensile tests after (a) direct heating (DH) pretreatment (RD, DD and TD) and (b) direct heating and superplastic pre-strain (DHS) pretreatment (RD). t_p and t_s are the pre-straining duration and the subsequent soak (Table 2).

Tests were performed using a Gleeble 3800 thermo-mechanical testing system in ambient air without protective gas. A pair of K-type thermocouple wires was spot welded at the centre of the parallel section to measure the temperature of the parallel section, which was controlled by direct resistance heating and compressed-air cooling in a closed loop. Force was measured by a load cell at the stationary jaw. Because the parallel section is heated by its own resistance between water-cooled grips, it carries an axial temperature gradient and deformation concentrates near its centre; strain was therefore measured locally, as described below, and the strain rate quoted is the nominal value programmed from the effective gauge length. After the prescribed DHS pre-strain, trial tests were used to recalibrate the effective gauge length of the pre-strained specimen for the strain-rate control of the subsequent test. Tests at each condition were repeated, and the peak stress agreed within 2% between repeats [25]; representative curves are shown. After fracture the specimens were cooled to room temperature at 50 °C s^{-1}.

Strain was measured with the contactless method detailed in [25], during both the pre-strain and the final test. Locally measured or locally controlled tests are needed for resistance-heated sheet specimens because the non-uniform temperature field produces non-uniform strain and strain-rate distributions along the gauge [48]. A high-speed camera recorded the specimen silhouette against a black background with an auxiliary light source at 500 frames s^{-1}. The images were rotated so that the upper edge of the undeformed parallel section was horizontal. A Sobel filter identified the specimen edge from the image grey levels [49]. Spurious edge positions caused by local oxide peeling were rejected using a threshold comparison between neighbouring pixels and replaced by interpolation. A reference point on the upper edge was matched to the lower edge within a horizontal distance of three pixels, and the separation of the selected edge positions defined the local width.

The width history was converted to true strain using the width-based method of Li et al [50]. The strain signal was smoothed with a Gaussian-weighted moving average over 30 frames [51], which at 500 frames s^{-1} and 1 s^{-1} corresponds to a window of 0.06 s, or about 0.06 strain, before differentiation. The image sequence and force record were synchronised using the frame showing complete fracture and the zero-force point. The width W corresponding to a local true strain ε was obtained from

$$W = W_0 \, exp\left(\frac{-\varepsilon}{2}\right) \tag{1}$$

where W_0 is the reference width for the stage considered (the undeformed width for the DH tests and the width after pre-straining and unloading for the DHS tests). The true stress σ was calculated from the force and the cross-sectional area obtained under the same assumption, and the same relation was used to select the locations for post-test microstructure characterisation. Flow softening was quantified by the normalised strain hardening rate

$$\gamma' = \frac{d \ln \sigma}{d\varepsilon} = \frac{1}{\sigma}\frac{d\sigma}{d\varepsilon} \tag{2}$$

where negative values indicate softening and a less negative value a lower softening rate.

Equation 1 assumes plastic volume conservation and equal width and thickness strains, i.e. a plastic strain ratio $r = 1$. For a general r the axial strain is $\varepsilon = -(1 + 1/r) \ln(W/W_0)$ rather than $-2 \ln(W/W_0)$, and the cross-sectional area used for the true stress changes correspondingly. Propagating both effects, the normalised softening rate obtained with $r = 1$, γ'_1, is related to the value for a general r by

$$\gamma' = \frac{2\gamma'_1 - (1 - 1/r)}{1 + 1/r} \quad (3)$$

The relation is monotonic in γ'_1, so the ranking of the conditions compared below is independent of r provided that the conditions compared share a similar r. The magnitude of a difference is not, and the percentage changes quoted later are conditional on $r = 1$ (see 4.3).

2.3. Microstructure characterisation

Locations corresponding to selected local true strains were marked along the parallel sections with reference to the widths from Equation 1, and microstructures were examined at these locations in the quenched specimens after fracture. The maps therefore represent spatially sampled end states rather than an interrupted-test sequence on one region. Because of the axial temperature gradient, positions of lower local strain lie further from the specimen centre and deformed at a lower temperature, so comparisons between conditions are made at equal local strain and hence at similar positions. An ATM Brillant 220 cut-off machine with an abrasive wheel was used to remove the selected regions, which were hot mounted for metallographic preparation of the sheet plane (RD-TD). Samples were ground using an ATM Saphir 520 machine with P800, P1200, P2500 and P4000 SiC papers, and final polishing used MetPrep Chemicloth M and a mixture of 70% 0.06 μm colloidal silica suspension and 30% hydrogen peroxide for 1 h.

A Tescan Clara scanning electron microscope (SEM) equipped with a backscattered electron detector and an Oxford Symmetry EBSD detector was used for characterisation. SEM images were taken in backscattered electron (BSE) mode. EBSD scans were acquired at 25 kV and 10 nA with a step size of 0.5 μm for texture and macrozone characterisation and 0.2 μm for the analysis of deformation substructure. An area of 400 × 300 μm was acquired for each EBSD mapping. Inverse pole figure (IPF) maps are coloured with respect to the normal direction (ND). The as-received sheet consisted of equiaxed primary α (α_p) grains and β phase (Fig. 3). The IPF map and pole figures in Fig. 4 show macrozones formed by clusters of similarly oriented α grains, and a strong texture with a maximum basal-pole intensity of 18 multiples of random distribution (MRD), with most basal poles close to TD.

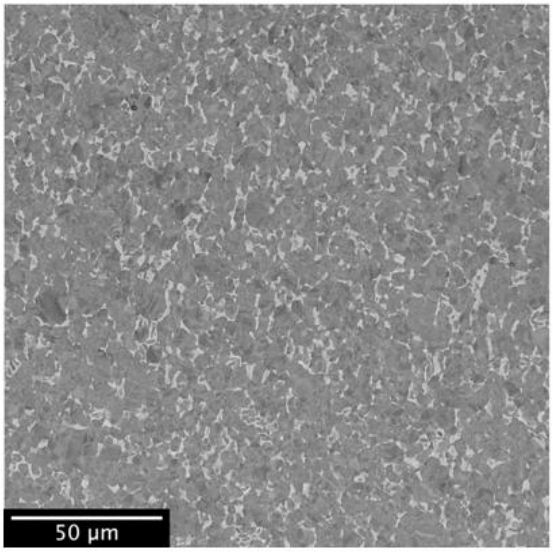

Fig. 3. SEM micrograph (BSE mode) of the as-received sheet (α phase dark, β phase light).

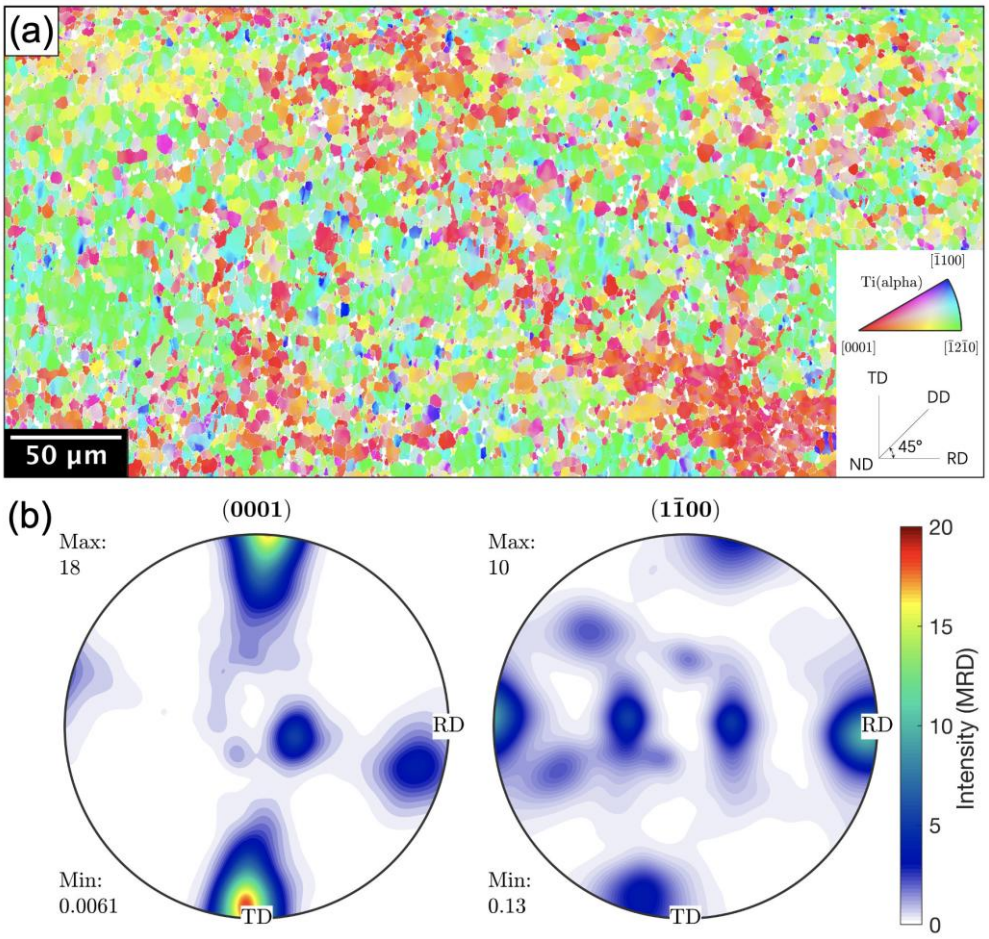

Fig. 4. (a) EBSD inverse pole figure (IPF) map with respect to ND and (b) (0001) and {1$\bar{1}$00} pole figures of the as-received sheet, showing macrozones and a strong texture. RD is horizontal and TD vertical in the pole figures.

Quenching retained the primary α grains while the high-temperature β phase transformed to a fine acicular product with lath widths of about 0.2 μm. Indexed α objects smaller than three pixels were excluded to reduce the contribution of this transformed constituent. The retained α population is treated as predominantly primary α: the filter does not achieve complete phase separation, and because its physical size (1.5 μm at the 0.5 μm step, and 0.6 μm at the 0.2 μm step) depends on the step size, more of the fine transformed phase survives in the 0.2 μm maps. Maximum pole intensities and average GND densities are therefore compared only between maps acquired with the same step size and filter. For example, the difference between the 18 MRD of the as-received sheet (0.5 μm step, Fig. 4) and the 8.5 MRD of the heat-treated reference state (0.2 μm step, see 3.4) should not be interpreted directly as evidence of texture evolution during the 300 s soak, since the two datasets differ in step size, filtering threshold and sampled map area.

Grain orientation spread (GOS), the average deviation of point orientations from the mean grain orientation, was used to separate low- and high-orientation-spread grain populations with an operational threshold of 2° [25]. Low-angle grain boundaries were defined by misorientations between 2° and 15° and high-angle boundaries by misorientations above 15°. Low GOS was considered alongside grain morphology and boundary character when discussing recrystallisation.

The EBSD-derived GND density was used to examine lattice-curvature-related plastic heterogeneity [52,53]. Following Nye's dislocation tensor formulation [54], the lattice curvature obtained from EBSD gives the dislocation content associated with orientation gradients [55]. The elastic strain gradient was assumed to be small relative to the lattice rotation gradient, and GND densities were estimated using the approach of Pantleon [56]. Calculations were implemented in MATLAB using MTEX with a basis of 33 dislocation types [53]; the optimisation minimised the total dislocation line energy, with the line-energy weight of ⟨c+a⟩ edge dislocations 3.5 times that of ⟨a⟩ edge dislocations [53] and the ratio of ⟨a⟩ edge to ⟨a⟩ screw line energies equal to $1/(1 - \nu)$, where ν is Poisson's ratio [57]. Only in-plane orientation gradients were measured, so the fitted GND content is an estimate derived from two-dimensional EBSD data rather than the total dislocation density; its noise floor and magnitude depend on the step size [58], which is a further reason for comparing only maps of identical step size. The plotted dislocation-family ratio, $\log_{10}(\rho\langle a\rangle/\rho\langle c+a\rangle)$, was used only as a relative indicator within the adopted inversion: positive values indicate a larger inferred ⟨a⟩ contribution

and negative values a larger inferred ⟨c+a⟩ contribution. The inversion does not identify uniquely which slip systems were active.

3. Results

3.1. Anisotropic flow after direct heating

The DH flow curves exhibited an early peak stress followed by continuous flow softening in all three loading directions (Fig. 5a). DH-TD had the highest peak stress (about 190 MPa) and the lowest local fracture strain; DH-DD flowed at a slightly higher stress than DH-RD after the peak and reached the largest local fracture strain. Fig. 5b shows the normalised strain hardening rate, γ' (Equation 2). The initial softening of DH-RD and DH-DD diminished as strain increased, and γ' reached its least negative values at strains of about 0.24 and 0.18, respectively; DH-TD showed less pronounced softening at the earliest stage and reached its least negative γ' at about 0.15. Above a true strain of 0.05, DH-DD softened less than DH-RD and DH-TD, whereas DH-TD softened most rapidly above about 0.3. These directional differences provided the basis for the microstructural comparisons below.

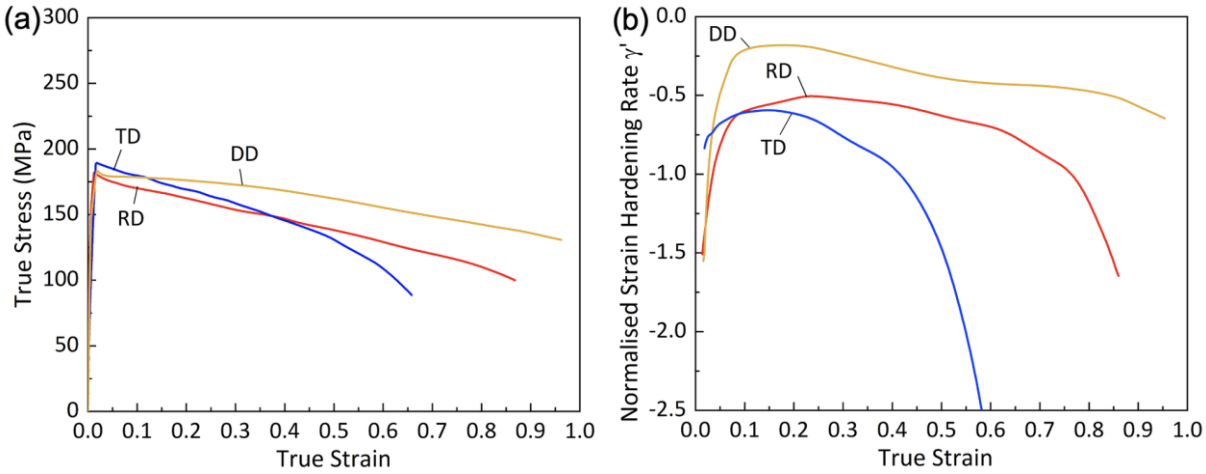

Fig. 5. (a) Flow stress and (b) normalised strain hardening rate γ' of the material tested after DH pretreatment along RD, DD and TD.

3.2. Grain morphology and texture after direct heating

The post-test SEM micrographs of the DH specimens shown in Fig.6 revealed clusters of primary α grains with different aspect ratios. Most grains in DH-RD were elongated compared to the as-received state, although groups of grains with lower aspect ratios remained. Clusters of elongated grains were also present in DH-DD and DH-TD. The DH-TD microstructure contained a greater prominence of globular, comparatively large primary α grains than DH-DD.

The co-existence of differently deformed grain clusters is consistent with heterogeneous deformation associated with the macrozone structure.

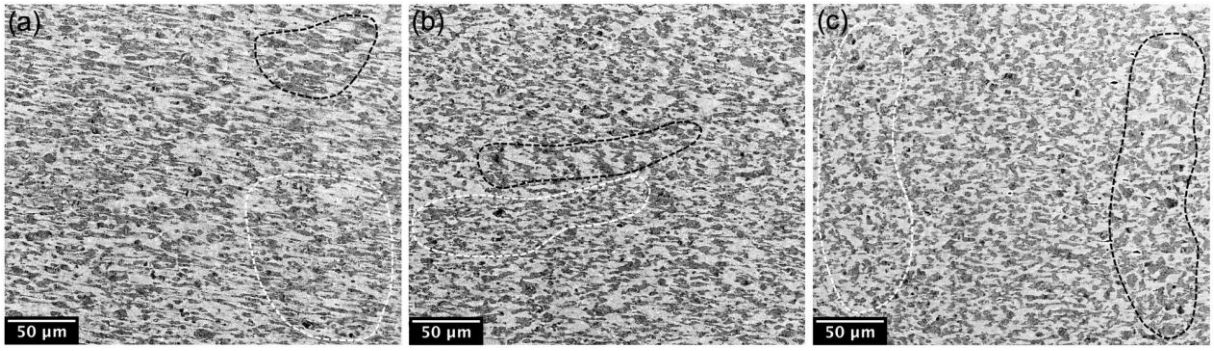

Fig. 6. SEM microstructures after DH tests along (a) RD, (b) DD and (c) TD after fracture; the tensile axis is horizontal. Dashed white outlines mark representative clusters of primary α grains with high aspect ratios and dashed black outlines clusters with low aspect ratios.

Fig. 7 compares IPF maps and basal pole figures at local true strains of 0.15, 0.25 and 0.5 of the DH specimens. Similarly oriented grain clusters remained visible at strains of 0.15 and 0.25 in all three loading directions, whereas the maps at 0.5 showed markedly reduced orientation clustering. In DH-RD the maximum basal-pole intensity decreased from 9.9 MRD at strain 0.15 to 6.1 MRD at 0.25 and 5.0 MRD at 0.5, with a broader pole distribution at the higher strain. In DH-DD it decreased from 7.4 MRD at 0.15 to 7.2 MRD at 0.25 and 4.1 MRD at 0.5, and at the highest strain the basal poles formed a broad band along DD. In DH-TD (6.5, 6.0 and 4.0 MRD at the three strains), a narrower band along RD was visible at 0.25, corresponding to grains with c-axes approximately perpendicular to the tensile axis, and the distribution was substantially more dispersed at 0.5. The evolution of texture therefore differed between loading directions as well as with local strain.

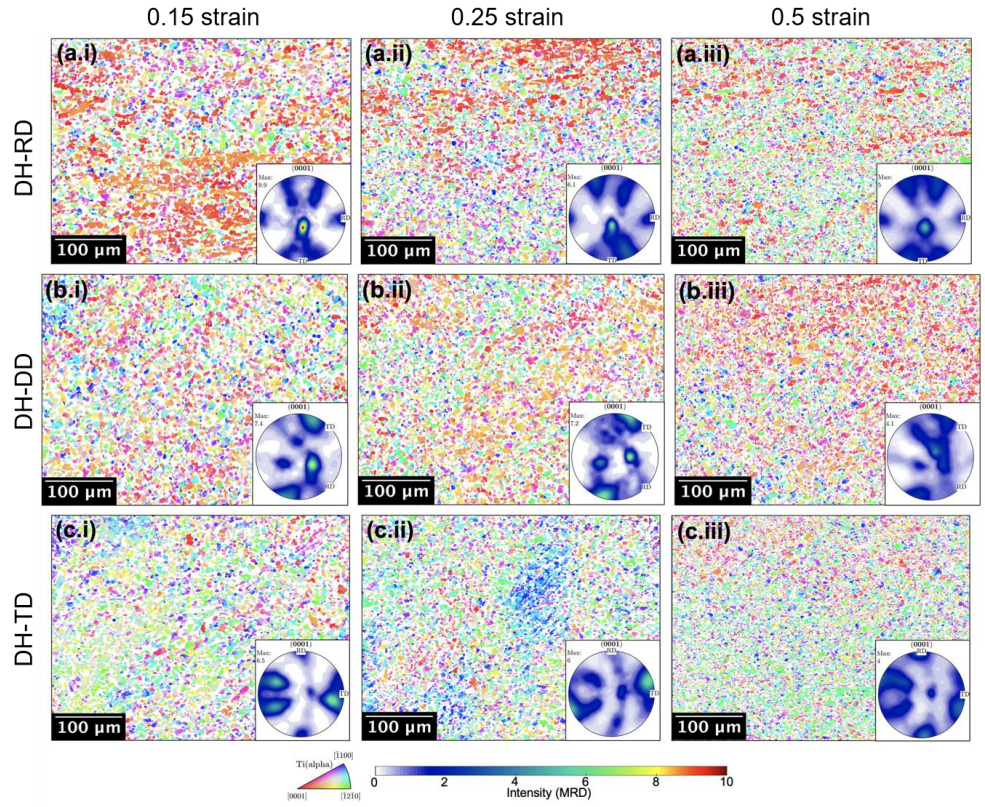

Fig. 7. EBSD (0.5 µm step) IPF maps and (0001) pole figures after DH tests along (a) RD, (b) DD and (c) TD at local true strains of (i) 0.15, (ii) 0.25 and (iii) 0.5. The pole figures are plotted in the specimen frame of each test, with RD and TD marked.

3.3. Slip-system favourability and dislocation structure after direct heating

The Schmid-factor maps in Fig. 8 and distributions in Fig. 9 describe the geometric favourability of basal ⟨a⟩ and prismatic ⟨a⟩ slip for each loading direction at a local strain of 0.25, the strain at which γ' is least negative and therefore the orientation state most relevant to the softening being interpreted. They are read as continuous orientation distributions without a universal activation threshold: a high Schmid factor does not establish activation, because local stress, grain-neighbour interactions and slip resistance also matter [32,59–61]. Basal and prismatic ⟨a⟩ slip were examined because ⟨c+a⟩ slip has a greater activation resistance under hot-working conditions [62]. In DH-RD, clusters of α_p grains with low basal Schmid factors have high prismatic Schmid factors (Fig. 8a), and the prismatic distribution in Fig. 9a peaks at about 0.45. DH-DD shows a more balanced distribution: relatively few grains have near-zero values for either slip family, and regions favourable for basal slip also carry appreciable prismatic Schmid factors (Figs. 8b and 9b). In DH-TD, a large region has low basal and near-

zero prismatic Schmid factors (Fig. 8c), and the prismatic distribution in Fig. 9c peaks near 0.05.

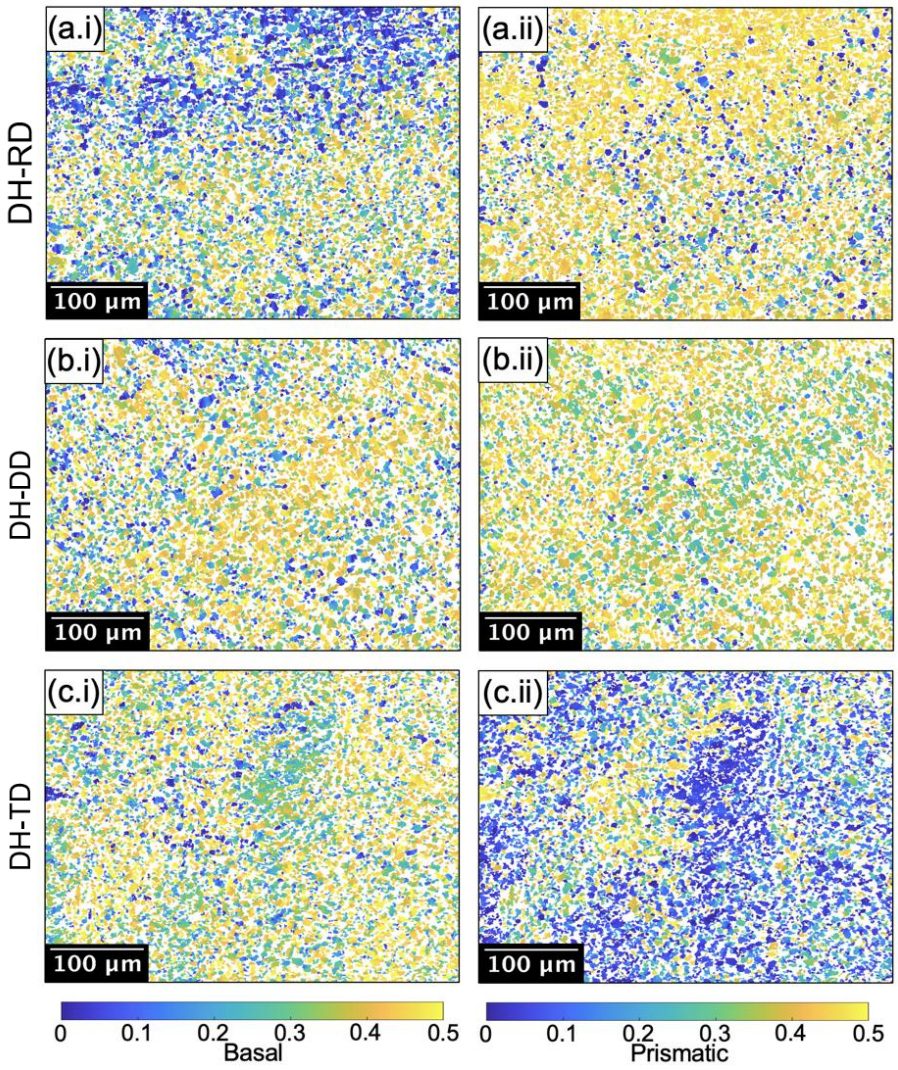

Fig. 8. Schmid factor maps after DH tests along (a) RD, (b) DD and (c) TD at a local strain of 0.25, for (i) basal ⟨a⟩ and (ii) prismatic ⟨a⟩ slip.

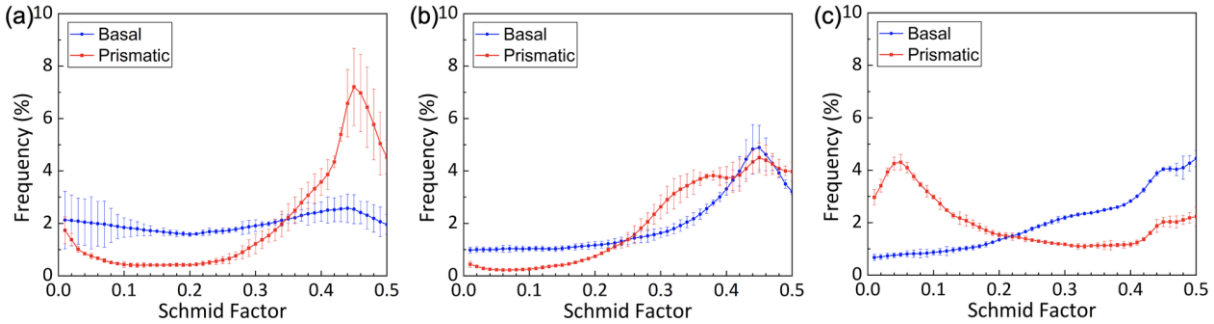

Fig. 9. Distributions of Schmid factors for basal ⟨a⟩ and prismatic ⟨a⟩ slip at a local strain of 0.25 after (a) DH-RD, (b) DH-DD and (c) DH-TD tests. Error bars indicate the standard deviation.

The DH-DD maps at a local strain of 0.15 in Fig. 10 show heterogeneous lattice-curvature-related dislocation storage. Bands of elevated GND density (Fig. 10b), of order 10^{15} m^{-2}, and low-angle boundaries divide some α_p grains into cell-like regions against a background of order 10^{14} m^{-2}. Band traces extend across adjacent grains (dashed line), and the grain (circled) in Fig. 10b combines a high GND density with a mixture of positive and negative family-ratio values (Fig. 10c).

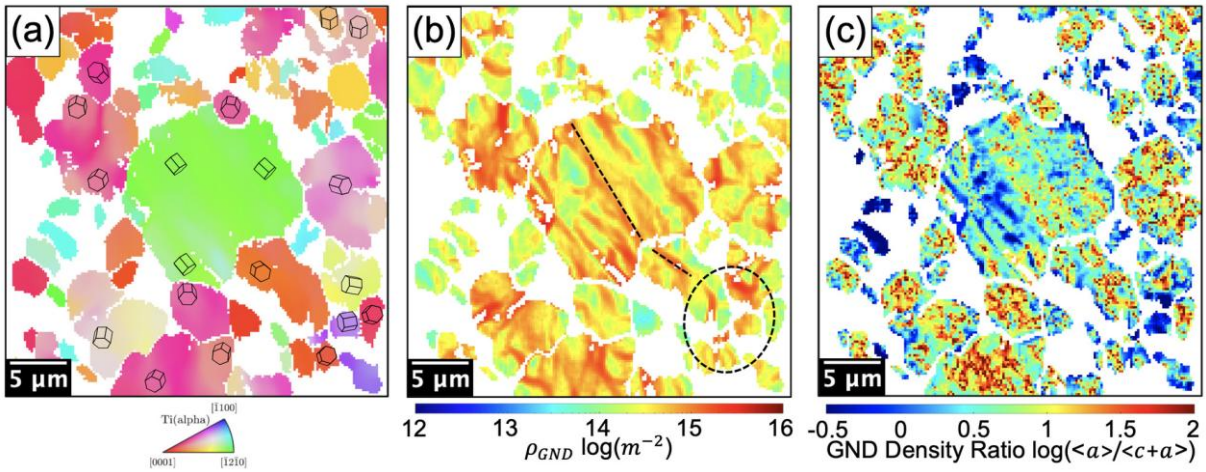

Fig. 10. EBSD (0.2 µm step) (a) IPF map, (b) GND density map and (c) GND density ratio map, $\log_{10}$ (ρ⟨a⟩/ρ⟨c+a⟩), of the material after the DH-DD test at a local strain of 0.15. The dashed line in (b) marks a band of elevated GND density crossing adjacent grains; the dashed circle marks a grain with high GND density and mixed family-ratio values.

3.4. Microstructure after superplastic pre-straining

Fig. 11 summarises the state of the material after DHS pretreatment as a function of pre-strain, with the DH-treated material (pre-strain 0) as the reference; all maps were acquired at the 0.2 µm step. The maximum (0001) pole intensity decreased from 8.5 MRD at zero pre-strain to 6.7, 6.0, 4.7 and 4.2 MRD at pre-strains of 0.15, 0.24, 0.5 and 1.0 (Fig. 11a), with a smaller further decrease above 0.5. The average GND density decreased from 5.75 × 10^{14} m^{-2} to 4.5, 3.5, 3.1 and 2.6 × 10^{14} m^{-2} (Fig. 11b). The circle-equivalent diameter of the primary α grains decreased slightly, from 6.02 µm to 5.94, 5.62, 5.48 and 5.20 µm (Fig. 11c). The fraction of low-angle boundaries (2-15°) fell from 63.2% to 45.3%, 38.0%, 31.1% and 22.2%, with a corresponding rise in the fraction of high-angle boundaries (Fig. 11d). The 0.5 and 1.0 states are therefore treated as ancillary characterisation points because their longer total times at 900 °C preclude direct attribution of the additional changes solely to pre-strain (Table 2).

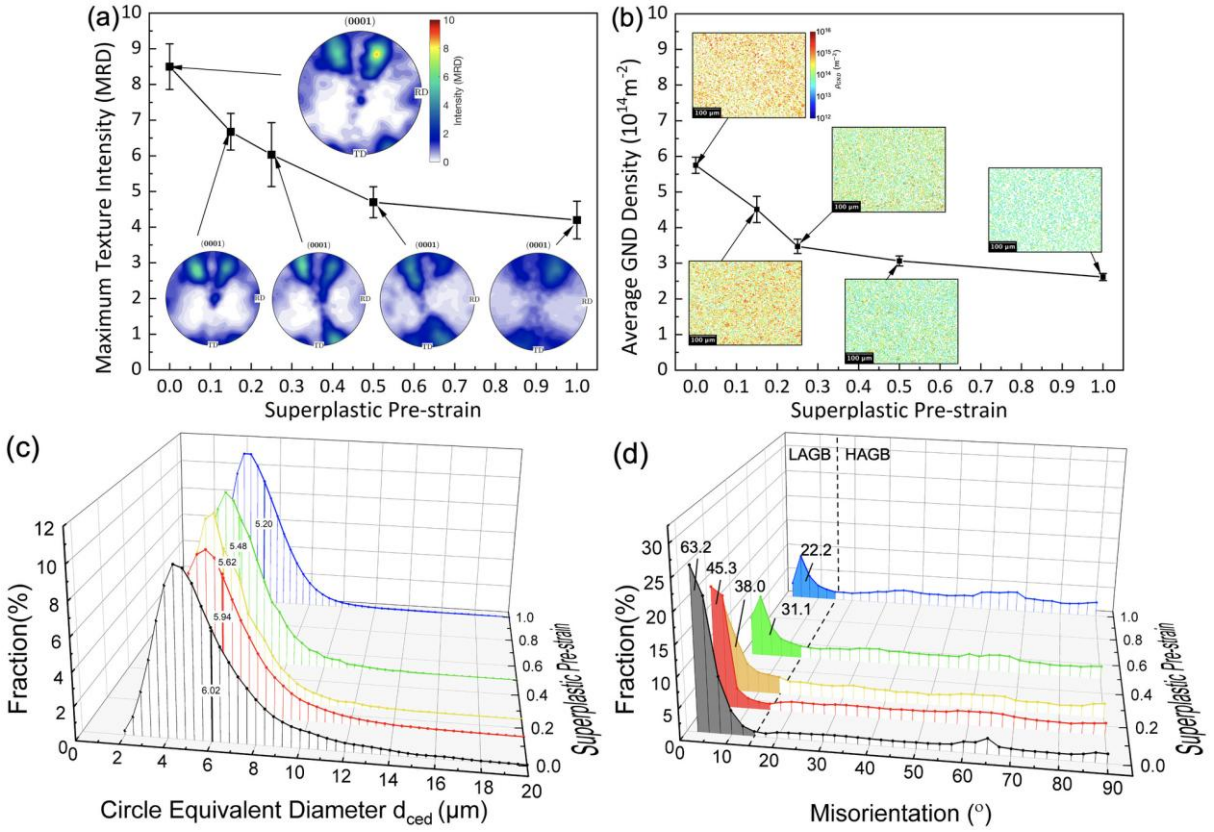

Fig. 11. (a) Maximum (0001) pole intensity, (b) average GND density, (c) circle-equivalent diameter of the primary α grains and (d) grain boundary misorientation distribution of the material after DHS pretreatment to pre-strains of 0 (DH reference), 0.15, 0.24, 0.5 and 1.0 (0.2 μm step). The 0.5 and 1.0 states had a longer total time at 900 °C. Error bars indicate the standard deviation.

3.5. Flow behaviour after pre-straining

Fig. 12 compares the flow curves and γ' of DH-RD (pre-strain 0), DHS-0.15-RD and DHS-0.24-RD, all tested along RD; strain is the local true strain of the final test measured from the pre-strained and unloaded state. The peak stress increased with pre-strain, from about 183 MPa to about 190 and 200 MPa. Both pre-strained conditions softened less than DH-RD during the early stage. At a strain of 0.2, γ' was -0.52 for DH-RD, -0.39 for DHS-0.15-RD and -0.272 for DHS-0.24-RD, and DHS-0.24-RD reached its least negative value, -0.243, at a strain of 0.26. The reduction in the magnitude of γ' at a strain of 0.2, (0.520 - 0.272)/0.520 = 48%, is a point estimate under reconstruction. The advantage was strain-dependent: γ' of DHS-0.24-RD fell below that of DH-RD at a strain of about 0.45, and that of DHS-0.15-RD at about 0.6. The local fracture strain was about 0.87 for DH-RD, 0.85 for DHS-0.15-RD and 0.75 for DHS-0.24-RD, and the flow stress of DHS-0.24-RD crossed below that of DH-RD at a strain of about 0.7.

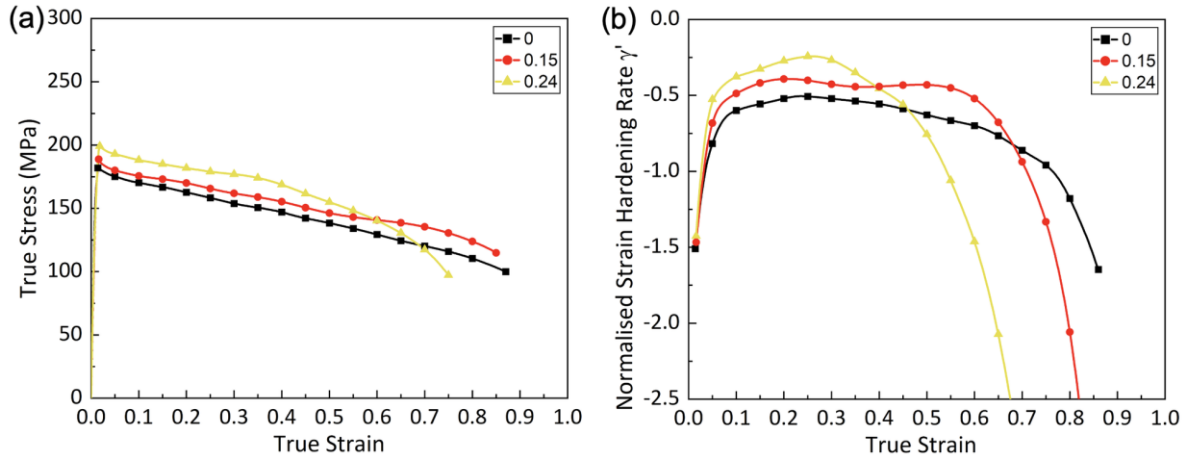

Fig. 12. (a) Flow stress and (b) normalised strain hardening rate γ' of the material tested along RD after DH (pre-strain 0) and DHS pretreatment (pre-strains 0.15 and 0.24). Strain is the local true strain of the final test, measured from the pre-strained and unloaded state.

3.6. Dislocation storage after pre-straining

The EBSD comparison at a local strain of 0.15 (Fig. 13) shows a less clustered orientation arrangement in DHS-0.24-RD than in DH-RD (Fig. 13a), together with higher GND densities in the pre-strained material (Fig. 13b). The family-ratio map of DHS-0.24-RD contains a more balanced distribution of positive and negative values than that of DH-RD (Fig. 13c). The average GND density (Fig. 14) was lower in the pre-strained material before the final test (see 3.4) but higher after it: at local strains of 0.15 and 0.25 it was about 7.5 and 8.9 × 10^{14} m^{-2} for DH-RD, 9.6 and 10.3 × 10^{14} m^{-2} for DHS-0.15-RD and 10.3 and 11.4 × 10^{14} m^{-2} for DHS-0.24-RD, and 11.0 × 10^{14} m^{-2} for DH-RD at a strain of 0.5. The increase over the sampled strain interval was therefore largest for DHS-0.24-RD. Because the maps were sampled from different locations in fractured specimens, this is a comparison against local strain rather than a directly measured accumulation rate.

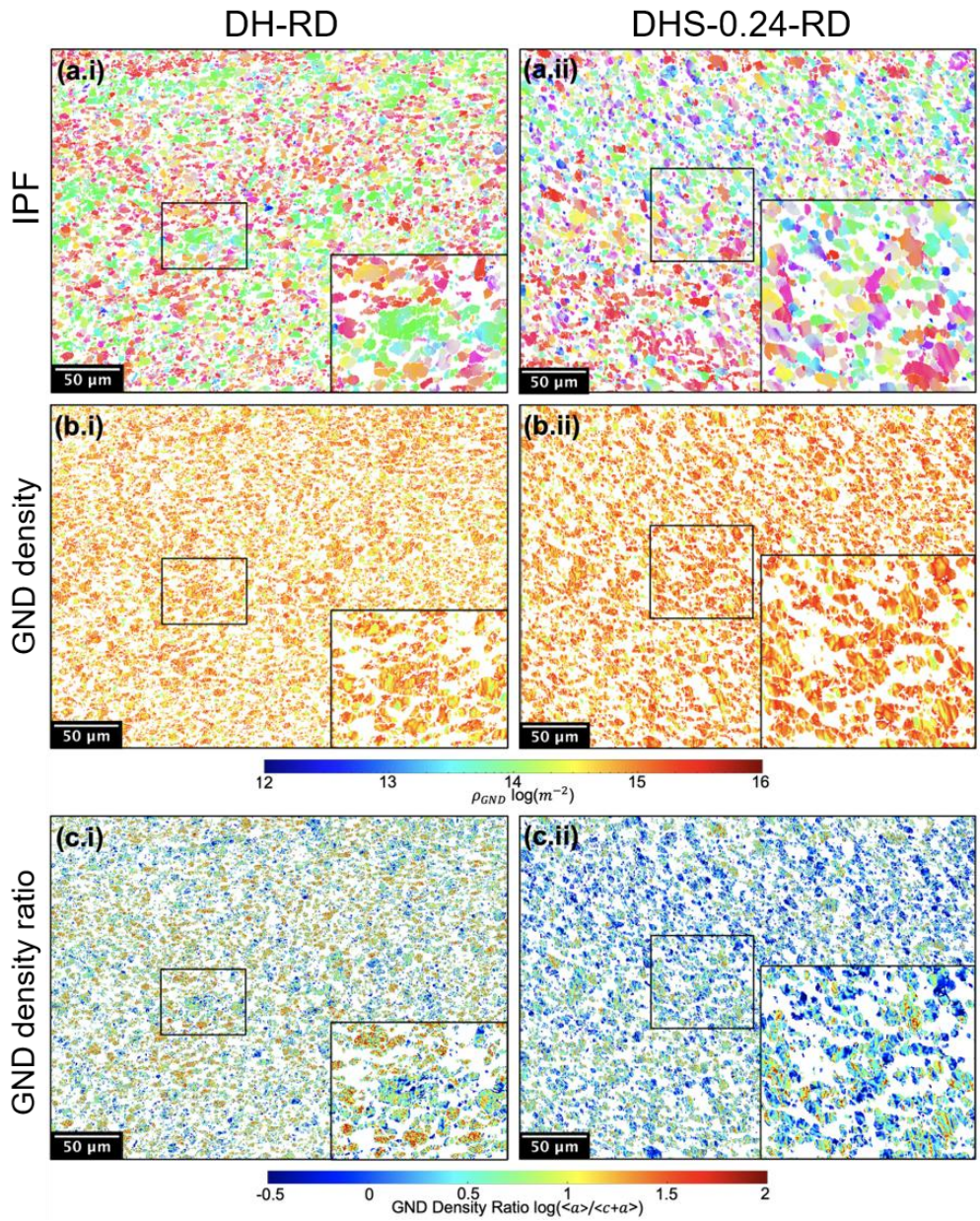

Fig. 13. EBSD (0.2 µm step) (a) IPF map, (b) GND density map and (c) GND density ratio map of the material after (i) the DH-RD test and (ii) the DHS-0.24-RD test at a local strain of 0.15.

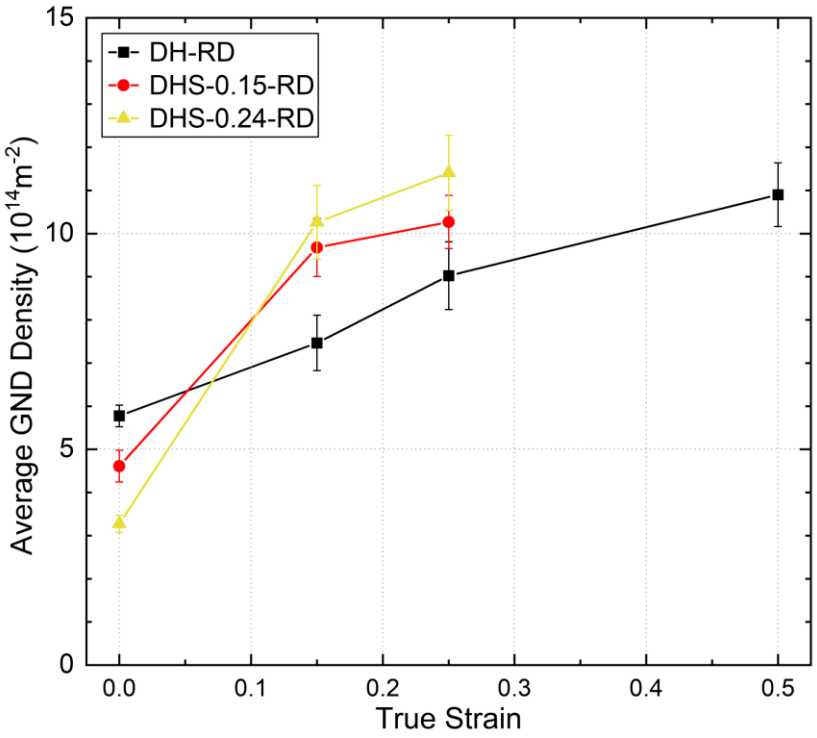

Fig. 14. Average GND density against the local true strain of the final test after DH and DHS pretreatments (0.2 μm step). Points are map averages from different positions of fractured specimens; lines guide the eye. Error bars indicate the standard deviation.

4. Discussion

4.1. Origin of the anisotropic flow

The directional differences in flow stress and softening at 900 °C and 1 s^{-1} reflect the balance between dislocation accumulation and the mechanisms that reduce deformation resistance. Dislocation multiplication contributes to work hardening [63], whereas recovery, recrystallisation and dynamic phase transformation contribute to softening [10]; deformation heating and changes in crystallographic orientation also affect the measured response (see 4.2). At the subtransus deformation temperature both α_p grains and a substantial β phase fraction accommodate plastic deformation, and the relatively soft β phase is expected to contribute substantially during the early stage [17,64]. Compatibility between deformation in the two phases depends partly on their crystallographic relationship: where the Burgers orientation relationship is satisfied, $\{110\}\beta \parallel \{0001\}\alpha$ and $\langle 111\rangle\beta \parallel \langle 11\bar{2}0\rangle\alpha$, compatible slip systems can facilitate slip transfer across α/β interfaces, whereas a departure from it obstructs transfer through the misalignment of slip vectors [26]. An unfavourably oriented α_p grain can likewise obstruct slip originating in an adjacent favourably oriented grain [36]. Both the orientation of

individual grains and the spatial arrangement of neighbouring grains may therefore affect dislocation storage.

The Schmid-factor distributions (Figs. 8 and 9) rationalise the ranking of the three directions. With most basal poles close to TD (Fig. 4), loading along TD places many grains with the c-axis near the tensile axis, for which neither basal nor prismatic ⟨a⟩ slip is favourably oriented; the higher peak stress of DH-TD and an increased importance of ⟨c+a⟩ slip, and local shear accommodation follow [13]. Loading along RD favours prismatic ⟨a⟩ slip within similarly oriented clusters, which can accommodate deformation compatibly and contribute to strain heterogeneity between macrozones. The balanced distribution of DH-DD increases the likelihood of multiple slip and of dislocation interaction within the same grains, which promotes dislocation accumulation and is a possible reason for its lower softening rate. The GND maps of DH-DD (Fig. 10) support this reading: bands of elevated GND density crossing adjacent grains are consistent with slip transfer, with the difference in band direction reflecting the crystallographic geometry [65], and the mixed inferred ⟨a⟩ and ⟨c+a⟩ contributions in the circled grain are compatible with dislocation interaction and storage [66]. The analysis does not identify uniquely which slip systems were active.

Recovery and recrystallisation provide competing routes for reducing stored dislocations. The pole figures of the low- and high-GOS grain populations at a local strain of 0.25 (Supplementary Fig. S1) show related orientation distributions in all three directions, with the low-GOS population in DH-RD including orientations with c-axes towards RD and TD and a broader distribution than in DH-DD. A low GOS can arise in recovered or weakly deformed grains as well as in recrystallised ones. Neighbouring grains with compatible orientations may permit deformation over an effective structural length greater than an individual grain, whereas grains with less compatible orientations interrupt this path and increase the number of barriers encountered by slip. High-angle boundaries are expected to impede transmission more strongly than low-angle subgrain boundaries [67], and hard-oriented α_p grains can obstruct slip from adjacent softer grains [36,37]. A more dispersed orientation distribution may therefore shorten the effective slip length and promote storage; the maps estimate curvature-related dislocation content and do not measure the total dislocation population or the effective slip length directly.

4.2. Why pre-straining suppresses early softening

Pre-straining at 900 °C and 10^{-3} s^{-1} of the DHS specimens changed several features of the starting state together (Fig. 11): a weaker basal texture and less clustered orientations, consistent

with grain boundary sliding and grain rotation [2,40,41]; conversion of low-angle into high-angle boundaries and a slight grain refinement, consistent with continuous dynamic recrystallisation [9,42]; and a lower residual GND density, attributed to recovery during the slow deformation and the subsequent hold. Three candidate contributions to the lower early softening rate then need to be weighed.

An alternative to the orientation-dispersal interpretation must be considered first. The DH material contains a high fraction of low-angle boundaries (63%) after the thermal cycle, indicating a recovered substructure inherited from sheet processing, whereas the pre-strained material contains a higher fraction of high-angle boundaries and a lower residual GND density. Grains with less initial substructure may allow greater dislocations accumulation before recovery balances storage, and this alone would reduce the net softening rate irrespective of texture. The different post-strain holds (120 s for 0.15, 30 s for 0.24) are unlikely to be the sole explanation of the residual state: if static recovery during the hold dominated, the 0.15 route would have the lower residual GND density, whereas it has the higher (4.5 against 3.5×10^{14} m^{-2}).

Two observations favour an additional orientation-related contribution: the higher peak stress after pre-straining, which is unlikely to be accounted for by the ~7% grain refinement alone and is consistent with a larger fraction of grains unfavourably oriented for ⟨a⟩ slip along RD; and the shift of the inferred ⟨a⟩/⟨c+a⟩ ratio towards a more balanced distribution (Fig. 13c), which indicates a relatively greater involvement of ⟨c+a⟩-type curvature in the pre-strained material. Grain reorientation may also alter slip compatibility across α/β interfaces, but departures from the Burgers orientation relationship were not measured. The contributions are not separable with the present data, and the evidence is read as orientation dispersal and boundary-character change acting together to increase dislocation storage, which the larger GND accumulation of the pre-strained material over the sampled strain interval reflects (Fig. 14).

Deformation heating contributes to the softening of every curve and must be separated from these microstructural effects. At 1 s^{-1} a strain of 0.2 is reached in 0.2 s, so the gauge interior is close to adiabatic: the closed-loop control can reduce the heating current but heat removal from the gauge is limited over such a short interval. Assuming a Taylor–Quinney coefficient of 0.9, a value consistent with the inelastic heat fractions measured for Ti-6Al-4V hot deformation [68], a density of 4430 kg m^{-3} and a specific heat of about 775 J kg^{-1} K^{-1} at 900 °C [69], the adiabatic heating rate is

$$\frac{dT}{d\varepsilon} = \frac{0.9\sigma}{\rho c_p} \approx 45\ \mathrm{K}\, per\ unit\ strain \quad (4)$$

for $\sigma \approx 175$ MPa, i.e. about 9 K at a strain of 0.2 and 20 K at 0.5. With a temperature sensitivity of the flow stress of about 1.2-1.5 $MPaK^{-1}$ at this temperature and rate [10,11], fully adiabatic heating would contribute roughly -0.3 to γ', which is comparable with the measured values. Levkulich and Semiatin estimated a heating share of about 10% of the softening at 0.1 s^{-1} [27], and the share at 1 s^{-1} is expected to be larger [70]. Three consequences follow. Part of the softening common to all conditions is thermal, so the absolute values of γ' overstate the microstructural softening. The comparison between DH-RD and the pre-strained conditions is conservative with respect to heating, because the pre-strained material flows at a 5-10% higher stress and therefore heats faster, which would make it soften more, not less. And DH-TD carries the highest stress and hence the largest heating term, so its rapid softening above a strain of about 0.3 cannot be attributed to orientation alone.

Beyond a strain of about 0.45 (DHS-0.24-RD) or 0.6 (DHS-0.15-RD) the pre-strained material softens faster than DH-RD, and the 0.24 pre-strain lowers the local fracture strain from about 0.87 to 0.75. The development of intersecting subgrain boundaries and larger internal orientation gradients in the more heavily stored grains may promote further recrystallisation and contribute to this later softening. Cavities nucleated by grain boundary sliding during the pre-strain and grown during the fast stage, and the higher stress in the neck, are possible contributions to the earlier fracture, although neither was examined here. The 0.15 pre-strain offers a smaller early gain that persists to a larger strain with almost no loss of local fracture strain, so the two routes represent a trade-off rather than a monotonic improvement with pre-strain; the pre-strain-dependent response reported by Wu et al. under a different sequence [47] likewise cautions against treating 0.24 as a generally optimal value.

4.3. Significance for forming and limitations

The significance of γ' for forming follows from Hart's analysis of the tensile test [71]. In a rate-sensitive material, tensile flow is stable while $\gamma' + m \geq 1$, where $m = \partial \ln \sigma / \partial \ln \dot{\varepsilon}$ is the strain-rate sensitivity; beyond that point a cross-sectional non-uniformity grows at a rate proportional to $(1 - \gamma' - m)/m$. With $m \approx 0.15$-0.2 for Ti-6Al-4V at 900 °C and 1 s^{-1} [11,25], every condition tested here is unstable from the peak stress onwards, which is why strain was measured locally rather than assumed uniform. The change in γ' at a strain of 0.2 from -0.52 (DH-RD) to -0.27 (DHS-0.24-RD) does not restore stability, but it reduces the neck-growth rate by roughly 20%, slowing strain localisation during the early stage that governs the thinning distribution in a

stamping stroke lasting a fraction of a second. The strain of 0.2 at which the comparison is made corresponds, under the assumptions of Equation 1, to about 10% thinning. For hot stamping of high-strength steel, thinning above 15% is commonly considered unacceptable [72], although this is not directly transferable to Ti-6Al-4V.

From a processing perspective the pre-strain is a conditioning step that could be applied as a slow pre-stretch or as a separate pre-forming operation on the blank, with the pre-strain path and magnitude chosen so that the conditioned blank remains within its forming limit; the strain-path dependence of the high-temperature forming limits of Ti-6Al-4V sheet [73] and coupled deformation–damage models for hot sheet forming of the alloy [74] provide the means to assess such a two-stage path. Its cost is the time at temperature (150-240 s at 900 °C in air, with the potential oxidation and alpha-case growth), a 5-10% higher flow stress during the fast stage and, for the larger pre-strain, a lower local fracture strain. Under the isotropic assumption of Equation 1, a uniaxial pre-strain of 0.24 alone corresponds to a thickness ratio of exp(-0.12) = 0.89, i.e. about 11% thinning before the fast stage; the pre-strain therefore consumes thickness that would otherwise be available to the component and cannot be treated as free deformation capacity. The present results demonstrate an early-stage benefit for the two pre-strains examined (0.15 and 0.24), persisting to subsequent strains of approximately 0.6 and 0.45, respectively. They do not establish an optimum pre-strain or a processing window.

Several limitations bound the interpretation. Strain and stress were reconstructed from the local width assuming isotropic contraction, so the absolute strain coordinates and the 48% figure are conditional on that assumption, although the ordering of the conditions is not; for r = 1.5, for example, Equation 3 reduces the 48% to about 36%. Deformation heating contributes to the softening of every condition. Because the parallel section carries an axial temperature gradient, positions of lower local strain lie further from the centre and deformed somewhat cooler, so the strain series in Figs. 7 and 14 carries a temperature component; comparisons between conditions are made at equal local strain and therefore at similar positions. The EBSD maps were taken from fractured, quenched specimens at positions assigned a local strain from Equation 1; they are spatially sampled end states rather than an interrupted-test sequence, and the fine transformed α' was reduced by a size filter rather than removed, so texture maxima and GND averages are compared only between maps acquired with the same step size. The GND densities are two-dimensional, model-dependent estimates of curvature-related dislocation content, and the ⟨a⟩/⟨c+a⟩ ratio is a relative indicator of the inversion rather than a measurement of slip activity. A single temperature and strain rate were examined, so the results are a focused case

study rather than a processing window. Finally, texture, grain size, boundary character and residual dislocation content changed together during the pre-strain and were not varied independently; the mechanistic reading above rests on the balance of evidence rather than on a controlled separation of these variables.

5. Conclusions

The influence of texture and macrozones on the hot flow of a textured Ti-6Al-4V sheet, and its alteration by superplastic pre-straining, were investigated by tensile testing at 900 °C and 1 s^{-1} after direct heating and after direct heating with superplastic pre-strain. The following conclusions are drawn.

1. At 900 °C and 1 s^{-1} the sheet is anisotropic: the transverse direction, along which most basal poles lie, has the highest peak stress, and the diagonal direction softens least. Post-test microstructures show differently deformed grain clusters, Schmid-factor distributions and localised GND bands observed in DH-DD consistent with heterogeneous deformation of the macrozones.
2. Superplastic pre-straining to 0.15 and 0.24 at 10^{-3} s^{-1} weakens the basal texture (from 8.5 MRD to 6.7 and 6.0 MRD), shifted the boundary population from low- towards high-angle boundaries (LAGB fraction 63% to 38%), slightly refines the primary α grains (6.0 to 5.6 μm) and lowers the residual GND density, consistent with continuous dynamic recrystallisation. The two pre-strain conditions had equal total time of 300 s at 900 °C but different post-strain holds (120 s and 30 s).
3. In the subsequent 1 s^{-1} deformation the pre-strained sheet shows a 5-10% higher peak stress and a lower normalised softening rate up to strains of 0.45 (pre-strain 0.24) and 0.6 (pre-strain 0.15), together with greater GND accumulation over the sampled strain interval; the 0.24 pre-strain lowers the local fracture strain from about 0.87 to 0.75.
4. The combined evidence is consistent with reduced orientation clustering and the change in boundary character acting together to increase dislocation storage during rapid deformation. Their individual contributions cannot be separated with the present data, and the role of the β phase remains unquantified.

Acknowledgements

The authors thank the Engineering and Physical Sciences Research Council for funding under grant EP/R001715/1 and acknowledge support from the UKRI Impact Acceleration Accounts (EP/X52556X/1) at Imperial College London. For the purpose of open access, the authors have applied a Creative Commons Attribution (CC BY) licence to any Author Accepted Manuscript version arising from this work.

CRediT authorship contribution statement

Famin Tian: Conceptualisation, Methodology, Investigation, Formal analysis, Validation, Visualisation, Writing - original draft. Hao Wu: Validation, Writing - review & editing. Nan Li: Conceptualisation, Supervision, Funding acquisition, Project administration, Writing - review & editing.

Data availability

The data supporting the findings of this study are available from the corresponding author on reasonable request.

Declaration of generative AI use

During the preparation of this work, the authors used ChatGPT (OpenAI) to assist with language editing, manuscript restructuring and literature checking. After using this tool, the authors reviewed, verified and edited the content as needed and take full responsibility for the content of the article.

References

[1] J.C. Williams, R.R. Boyer, Opportunities and issues in the application of titanium alloys for aerospace components, Metals (Basel). 10 (2020) 705. https://doi.org/10.3390/met10060705.

[2] T. Yasmeen, B. Zhao, J.H. Zheng, F. Tian, J. Lin, J. Jiang, The study of flow behavior and governing mechanisms of a titanium alloy during superplastic forming, Materials Science and Engineering: A 788 (2020). https://doi.org/10.1016/j.msea.2020.139482.

[3] E.L. Odenberger, M. Oldenburg, P. Thilderkvist, T. Stoehr, J. Lechler, M. Merklein, Tool development based on modelling and simulation of hot sheet metal forming of Ti-

6Al-4V titanium alloy, J. Mater. Process. Technol. 211 (2011). https://doi.org/10.1016/j.jmatprotec.2011.03.001.

[4] T. Maeno, M. Tomobe, K.I. Mori, Y. Ikeda, Hot stamping of titanium alloy sheets using partial contact heating, in: Procedia Manuf., 2018. https://doi.org/10.1016/j.promfg.2018.07.375.

[5] S. Chang, K. Wang, Z. Diao, Z. Li, S. Huang, G. Liu, Non-equilibrium hot stamping process for fully martensitic titanium alloy thin-walled components, Journal of Materials Research and Technology 39 (2025). https://doi.org/10.1016/j.jmrt.2025.10.209.

[6] K. Wang, M. Kopec, S. Chang, B. Qu, J. Liu, D.J. Politis, L. Wang, G. Liu, Enhanced formability and forming efficiency for two-phase titanium alloys by Fast light Alloys Stamping Technology (FAST), Mater. Des. 194 (2020). https://doi.org/10.1016/j.matdes.2020.108948.

[7] L. Yu, X. Yang, S. Liu, X. Huang, B. Wang, H. Ji, Stress relaxation behavior and springback prediction of Ti-6Al-4V alloy under triple-layer-sheet hot stamping condition, International Journal of Mechanics and Materials in Design 22 (2026). https://doi.org/10.1007/s10999-026-09874-9.

[8] J. Gupta, A. Arora, J. Singh, Advances in high-temperature deformation of titanium alloys: Experimental and modeling aspects for industrial applications, Materials Science and Engineering: A 948 (2025). https://doi.org/10.1016/j.msea.2025.149295.

[9] M. Qu, Z. Gu, X. Li, L. Yi, Y. Li, G. Yu, Y. Zhao, Hot Deformation Behavior and Microstructure Evolution Mechanisms of Ti6Al4V Alloy under Hot Stamping Conditions, Materials 17 (2024). https://doi.org/10.3390/ma17112531.

[10] M. Kopec, K. Wang, D.J. Politis, Y. Wang, L. Wang, J. Lin, Formability and microstructure evolution mechanisms of Ti6Al4V alloy during a novel hot stamping process, Materials Science and Engineering: A (2018). https://doi.org/10.1016/j.msea.2018.02.038.

[11] F. Tian, N. Li, Investigation of the feasibility of a novel heat stamping process for producing complex-shaped Ti-6Al-4V panel components, in: Procedia Manuf., 2020. https://doi.org/10.1016/j.promfg.2020.04.267.

[12] H. Wu, F. Tian, C. Tang, Z. Guo, N. Li, Novel Heat Stamping of Ti6Al4V panels with high drawability and low springback, MATEC Web of Conferences 401 (2024). https://doi.org/10.1051/matecconf/202440101012.

[13] S. Roy, S. Suwas, Orientation dependent spheroidization response and macro-zone formation during sub β-transus processing of Ti-6Al-4V alloy, Acta Mater. 134 (2017). https://doi.org/10.1016/j.actamat.2017.04.071.

[14] S. Gao, T. He, Q. Li, Y. Sun, Y. Sang, Y. Wu, L. Ying, Anisotropic behavior and mechanical properties of Ti-6Al-4V alloy in high temperature deformation, J. Mater. Sci. 57 (2022). https://doi.org/10.1007/s10853-021-06569-8.

[15] L. da Silva, G. Sivaswamy, L. Sun, S. Rahimi, Effect of texture and mechanical anisotropy on flow behaviour in Ti–6Al–4V alloy under superplastic forming conditions, Materials Science and Engineering: A 819 (2021). https://doi.org/10.1016/j.msea.2021.141367.

[16] X. Zeng, C.S. Daniel, W. Asheshov, S. Michalik, P. Prangnell, J. Quinta da Fonseca, Effect of Temperature, Strain and Microstructure on Texture Evolution of Ti-6Al-4V During Hot Rolling, Metall. Mater. Trans. A Phys. Metall. Mater. Sci. 56 (2025). https://doi.org/10.1007/s11661-025-07929-8.

[17] D. He, J.C. Zhu, Z.H. Lai, Y. Liu, X.W. Yang, An experimental study of deformation mechanism and microstructure evolution during hot deformation of Ti-6Al-2Zr-1Mo-1V alloy, Mater. Des. 46 (2013). https://doi.org/10.1016/j.matdes.2012.09.045.

[18] Z. Liu, P. Li, L. Xiong, T. Liu, L. He, High-temperature tensile deformation behavior and microstructure evolution of Ti55 titanium alloy, Materials Science and Engineering: A 680 (2017). https://doi.org/10.1016/j.msea.2016.10.095.

[19] X. Ji, B. Guo, F. Jiang, H. Yu, D. Fu, J. Teng, H. Zhang, J.J. Jonas, Accelerated flow softening and dynamic transformation of Ti-6Al-4V alloy in two-phase region during hot deformation via coarsening α grain, J. Mater. Sci. Technol. 36 (2020). https://doi.org/10.1016/j.jmst.2019.08.005.

[20] R. Ding, Z.X. Guo, A. Wilson, Microstructural evolution of a Ti-6Al-4V alloy during thermomechanical processing, Materials Science and Engineering: A 327 (2002). https://doi.org/10.1016/S0921-5093(01)01531-3.

[21] B. Babu, L.E. Lindgren, Dislocation density based model for plastic deformation and globularization of Ti-6Al-4V, Int. J. Plast. 50 (2013). https://doi.org/10.1016/j.ijplas.2013.04.003.

[22] S.L. Semiatin, T.R. Bieler, Effect of texture changes on flow softening during hot working of Ti-6Al-4V, Metall. Mater. Trans. A Phys. Metall. Mater. Sci. 32 (2001). https://doi.org/10.1007/s11661-001-0166-y.

[23] D. Li, X. Dong, H. Zhao, Y. Shen, Q. Yuan, R. Xu, J. Li, Y. Fan, C. Guo, S. Zhang, Dynamic recrystallization and texture evolution behavior of TC4 titanium alloy during hot deformation: Experiment and modeling, Materials Science and Engineering: A 957 (2026). https://doi.org/10.1016/j.msea.2026.149949.

[24] X. Du, J. Yang, S. Li, L. Wang, Y. Zheng, X. Zhang, Y. Liu, R. Chen, Competition between dynamic softening and hardening of Ti-6Al-4V alloy during hot deformation: Multi-mechanism coupling, J. Alloys Compd. 1080 (2026). https://doi.org/10.1016/j.jallcom.2026.190396.

[25] F. Tian, Development of a new heat stamping process for titanium alloy panel components, Imperial College London, 2023.

[26] S.L. Semiatin, T.R. Bieler, Effect of texture and slip mode on the anisotropy of plastic flow and flow softening during hot working of Ti-6Al-4V, Metall. Mater. Trans. A Phys. Metall. Mater. Sci. 32 (2001). https://doi.org/10.1007/s11661-001-0155-1.

[27] N.C. Levkulich, S.L. Semiatin, The Effect of Texture Evolution on Flow Softening During Hot Working of Ti-6Al-4V with a Colony Microstructure, Metall. Mater. Trans. A Phys. Metall. Mater. Sci. 56 (2025). https://doi.org/10.1007/s11661-025-07940-z.

[28] X. Cai, W. Zeng, H. Liu, Z. Hou, R. Jia, B. Wang, H. Li, Anisotropic impact response in Ti-6Al-4V alloy: crystallographic control of slip activation and macrozone during crack initiation and propagation, Materials Science and Engineering: A 948 (2025). https://doi.org/10.1016/j.msea.2025.149298.

[29] X. Zhang, D. Wei, S. Ma, T. Zhang, J. Sun, K. Li, X. Liu, G. Yu, S. Yang, Integrated in-situ experimental and crystal plasticity finite element investigation on grain-scale localized damage and fatigue prediction of forged Ti-6Al-4V alloy, Materials Science and Engineering: A 966 (2026). https://doi.org/10.1016/j.msea.2026.150328.

[30] D. Lunt, J.Q. da Fonseca, D. Rugg, M. Preuss, Microscopic strain localisation in Ti-6Al-4V during uniaxial tensile loading, Materials Science and Engineering: A 680 (2017). https://doi.org/10.1016/j.msea.2016.10.099.

[31] K. Kapoor, R. Noraas, V. Seetharaman, M.D. Sangid, Modeling Strain Localization in Microtextured Regions in a Titanium Alloy: Ti–6Al–4V, Integr. Mater. Manuf. Innov. 8 (2019). https://doi.org/10.1007/s40192-019-00159-y.

[32] D. Lunt, R. Thomas, M.D. Atkinson, A. Smith, R. Sandala, J.Q. da Fonseca, M. Preuss, Understanding the role of local texture variation on slip activity in a two-phase titanium alloy, Acta Mater. 216 (2021). https://doi.org/10.1016/j.actamat.2021.117111.

[33] L. Meng, T. Kitashima, P. Lin, L. Zheng, Z. Jiang, J. Zhao, In situ EBSD investigation of microtexture evolution and slip activation of α macrozones during tensile deformation in Ti-6Al-4V alloy, Materials Science and Engineering: A 924 (2025). https://doi.org/10.1016/j.msea.2024.147739.

[34] P.D. Littlewood, A.J. Wilkinson, Geometrically necessary dislocation density distributions in cyclically deformed Ti-6Al-4V, Acta Mater. 60 (2012). https://doi.org/10.1016/j.actamat.2012.07.003.

[35] A. Sarac, A. Bucsek, Slip system-specific critical resolved shear stress values and size effects for CP–Ti versus Ti–7Al, Materials Science and Engineering: A 959 (2026). https://doi.org/10.1016/j.msea.2026.149952.

[36] Z. Zheng, D.S. Balint, F.P.E. Dunne, Discrete dislocation and crystal plasticity analyses of load shedding in polycrystalline titanium alloys, Int. J. Plast. 87 (2016). https://doi.org/10.1016/j.ijplas.2016.08.009.

[37] S. Joseph, I. Bantounas, T.C. Lindley, D. Dye, Slip transfer and deformation structures resulting from the low cycle fatigue of near-alpha titanium alloy Ti-6242Si, Int. J. Plast. 100 (2018). https://doi.org/10.1016/j.ijplas.2017.09.012.

[38] Y. Kawano, M. Mitsuhara, T. Mayama, Anisotropy in stress-strain relationship in commercially pure titanium enhanced by deformation incompatibility, Materials Science and Engineering: A 952 (2026). https://doi.org/10.1016/j.msea.2025.149690.

[39] W. Changshun, L. Chenglin, H. Yuting, Z. Wenqiong, W. Danyang, L. Shiqi, Z. Guodong, Y. Bing, Microstructure-dependent slip activation and transfer governing the

strength-ductility synergy in L-PBF TC4 alloy, Materials Science and Engineering: A 971 (2026). https://doi.org/10.1016/j.msea.2026.150569.

[40] E. Alabort, D. Putman, R.C. Reed, Superplasticity in Ti-6Al-4V: Characterisation, modelling and applications, Acta Mater. 95 (2015). https://doi.org/10.1016/j.actamat.2015.04.056.

[41] J. Yang, J. Wu, Grain rotation accommodated GBS mechanism for the Ti-6Al-4V alloy during superplastic deformation, Crystals (Basel). 11 (2021) 991. https://doi.org/10.3390/cryst11080991.

[42] J. Yang, J. Wu, H. Xie, Z. Li, K. Wang, Mechanism of continuous dynamic recrystallization of Ti−6Al−4V alloy during superplastic forming with sub-grain rotation, Transactions of Nonferrous Metals Society of China (English Edition) 33 (2023). https://doi.org/10.1016/S1003-6326(23)66145-X.

[43] S. Xu, H. Zhang, N. Xiao, R. Qiu, Z. Cui, M. Fu, Mechanisms of macrozone elimination and grain refinement of near α Ti alloy via the spheroidization of the Widmannstätten structure, Acta Mater. 260 (2023). https://doi.org/10.1016/j.actamat.2023.119339.

[44] Y. Fan, X. Xue, X. Lu, Y. Shen, X. Zhang, J. Li, M. Lai, T. Luo, Synergistic enhancement of strength and plastic stability in near-α Ti-6Al-2.5V alloy via interstitial oxygen and macrozone fragmentation, Materials Science and Engineering: A 975 (2026). https://doi.org/10.1016/j.msea.2026.150898.

[45] B. Guo, H. Gao, C. Kong, Z. Wang, H. Cui, H. Yu, Transverse texture weakening and anisotropy improvement of Ti-6Al-4V alloy sheet via asymmetric rolling and static recrystallization annealing, J. Alloys Compd. 1010 (2025). https://doi.org/10.1016/j.jallcom.2024.177507.

[46] Y. Han, Y. Wang, Y. Meng, L. Cheng, W. Yu, X. Li, Texture evolution and mechanical anisotropy reduction in boron-microalloyed Ti-6Al-4V sheets during cold rolling and annealing, Materials Science and Engineering: A 953 (2026). https://doi.org/10.1016/j.msea.2025.149703.

[47] T. Wu, N. Wang, M. Chen, D. Zuo, L. Xie, W. Shi, Effect of pre-strain on microstructure and tensile properties of Ti-6Al-4V at elevated temperature, Metals (Basel). 11 (2021). https://doi.org/10.3390/met11081321.

[48] D. Naumann, M. Merklein, Beyond necking - Novel characterisation method to investigate the tensile response of sheet metals at elevated temperatures and constant true strain rates, Advances in Industrial and Manufacturing Engineering 12 (2026). https://doi.org/10.1016/j.aime.2026.100182.

[49] M.S. Nixon, A.S. Aguado, Low-level feature extraction (including edge detection), in: Feature Extraction and Image Processing for Computer Vision, 2026. https://doi.org/10.1016/b978-0-443-36686-4.00013-4.

[50] N. Li, C. Sun, N. Guo, M. Mohamed, J. Lin, T. Matsumoto, C. Liu, Experimental investigation of boron steel at hot stamping conditions, J. Mater. Process. Technol. 228 (2016). https://doi.org/10.1016/j.jmatprotec.2015.09.043.

[51] S.W. Smith, Moving Average Filters, in: The Scientist and Engineer's Guide to Digital Signal Processing, 2003.

[52] D. He, Q. Li, Y. Yan, X. Huang, T. Yasmeen, Study of plastic deformation mechanisms in TA15 titanium alloy by combination of geometrically necessary and statistically-stored dislocations, International Journal of Materials Research 107 (2016). https://doi.org/10.3139/146.111438.

[53] T. Ben Britton, S. Birosca, M. Preuss, A.J. Wilkinson, Electron backscatter diffraction study of dislocation content of a macrozone in hot-rolled Ti-6Al-4V alloy, Scr. Mater. 62 (2010). https://doi.org/10.1016/j.scriptamat.2010.01.010.

[54] J.F. Nye, Some geometrical relations in dislocated crystals, Acta Metallurgica 1 (1953). https://doi.org/10.1016/0001-6160(53)90054-6.

[55] T. Benjamin Britton, A.J. Wilkinson, Stress fields and geometrically necessary dislocation density distributions near the head of a blocked slip band, Acta Mater. 60 (2012). https://doi.org/10.1016/j.actamat.2012.07.004.

[56] W. Pantleon, Resolving the geometrically necessary dislocation content by conventional electron backscattering diffraction, Scr. Mater. 58 (2008). https://doi.org/10.1016/j.scriptamat.2008.01.050.

[57] D. Hull, D.J. Bacon, Introduction to Dislocations, 2011. https://doi.org/10.1016/s1369-7021(11)70217-6.

[58] J. Jiang, T.B. Britton, A.J. Wilkinson, Measurement of geometrically necessary dislocation density with high resolution electron backscatter diffraction: Effects of

detector binning and step size, Ultramicroscopy 125 (2013). https://doi.org/10.1016/j.ultramic.2012.11.003.

[59] F. Bridier, P. Villechaise, J. Mendez, Analysis of the different slip systems activated by tension in a α/β titanium alloy in relation with local crystallographic orientation, Acta Mater. 53 (2005). https://doi.org/10.1016/j.actamat.2004.09.040.

[60] B.R. Anne, Y. Okuyama, T. Morikawa, M. Tanaka, Activated slip systems in bimodal Ti–6Al–4V plastically deformed at low and moderately high temperatures, Materials Science and Engineering: A 798 (2020). https://doi.org/10.1016/j.msea.2020.140211.

[61] Y. Kawano, M. Sato, T. Mayama, M. Mitsuhara, S. Yamasaki, Quantitative evaluation of slip activity in polycrystalline α-titanium considering non-local interactions between crystal grains, Int. J. Plast. 127 (2020). https://doi.org/10.1016/j.ijplas.2019.12.001.

[62] A.A. Salem, S.L. Semiatin, Anisotropy of the hot plastic deformation of Ti-6Al-4V single-colony samples, Materials Science and Engineering: A 508 (2009). https://doi.org/10.1016/j.msea.2008.12.035.

[63] S.L. Semiatin, An Overview of the Thermomechanical Processing of α/β Titanium Alloys: Current Status and Future Research Opportunities, Metall. Mater. Trans. A Phys. Metall. Mater. Sci. 51 (2020). https://doi.org/10.1007/s11661-020-05625-3.

[64] S. Gao, Y. Sun, Q. Li, Z. Hao, B. Zhang, D. Gu, G. Wang, Research on the hot tensile deformation mechanism of Ti-6Al-4 V alloy sheet based on the α + β dual phase crystal plasticity modeling, J. Alloys Compd. 932 (2023). https://doi.org/10.1016/j.jallcom.2022.167701.

[65] J. Luster, M.A. Morris, Compatibility of deformation in two-phase Ti-Al alloys: Dependence on microstructure and orientation relationships, Metallurgical and Materials Transactions A 26 (1995). https://doi.org/10.1007/BF02670762.

[66] R. Shi, Z. Nie, Q. Fan, F. Wang, Y. Zhou, X. Liu, Correlation between dislocation-density-based strain hardening and microstructural evolution in dual phase TC6 titanium alloy, Materials Science and Engineering: A 715 (2018). https://doi.org/10.1016/j.msea.2017.12.098.

[67] S. Zaefferer, J.C. Kuo, Z. Zhao, M. Winning, D. Raabe, On the influence of the grain boundary misorientation on the plastic deformation of aluminum bicrystals, Acta Mater. 51 (2003). https://doi.org/10.1016/S1359-6454(03)00259-3.

[68] A. Raj, A. Ranjan, S. Nayak, K. Narasimhan, Investigation of inelastic heat fraction and its relationship to processing maps and microstructural evolution in Ti-6Al-4V during hot deformation, J. Alloys Compd. 1018 (2025). https://doi.org/10.1016/j.jallcom.2025.179035.

[69] M. Boivineau, C. Cagran, D. Doytier, V. Eyraud, M.H. Nadal, B. Wilthan, G. Pottlacher, Thermophysical properties of solid and liquid Ti-6Al-4V (TA6V) alloy, Int. J. Thermophys. 27 (2006). https://doi.org/10.1007/PL00021868.

[70] M. Kulakov, S. Rahimi, S.L. Semiatin, Effect of Deformation Heating on Microstructure Evolution During Hot Forging of Ti-6Al-4V, Metall. Mater. Trans. A Phys. Metall. Mater. Sci. 53 (2022). https://doi.org/10.1007/s11661-021-06493-1.

[71] E.W. Hart, Theory of the tensile test, Acta Metallurgica 15 (1967). https://doi.org/10.1016/0001-6160(67)90211-8.

[72] J. Cui, G. Sun, J. Xu, X. Huang, G. Li, A method to evaluate the formability of high-strength steel in hot stamping, Mater. Des. 77 (2015). https://doi.org/10.1016/j.matdes.2015.04.009.

[73] E. Gao, X. Liu, J. Wang, Q. Gao, R. Xu, Z. Zhu, High-temperature strain path effects on forming limits and microstructure of Ti-6Al-4V thin sheets, J. Alloys Compd. 1071 (2026). https://doi.org/10.1016/j.jallcom.2026.188822.

[74] D. Li, Z. Zhao, H. Hou, Z. Gao, J. Lv, K. Zheng, Integrated multi-scale framework for predicting deformation and damage in hot bulging of Ti-6Al-4V alloy: Experiments, modelling, and simulation, J. Mater. Process. Technol. 345 (2025). https://doi.org/10.1016/j.jmatprotec.2025.119067.